The Electric-Field Problem of an Interdigital Transducer in a Multilayered Structure

PETER M. VAN DEN BERG, WALTER J. GHIJSEN,
AND ADRIAN VENEMA, MEMBER, IEEE

Abstract—**A computational technique for the determination of the potential distribution of an interdigital transducer in a layered nonpiezoelectric environment is presented. Firstly, the problem is reduced to a dual boundary value problem for the potential distribution and the jump in the current density in the plane of the interdigital transducer. Secondly, an iteration scheme to solve this dual boundary value problem is outlined. It is based upon an iterative minimization of the integrated square error made in the boundary conditions on the transducer fingers. Finally, numerical results for some representative configurations are presented.**

I. Introduction

THE ANALYSIS OF surface acoustic wave (SAW) filters on silicon subtrates is of considerable importance for the design of these filters in integrated circuits (Fig. 1). Any analysis method of SAW devices is based upon the solution of the field equations and pertaining boundary conditions [1], [2]. This complicated problem is approximated either by methods using circuit models [3], [4] or a perturbational method using normal mode expansions [5]. In most cases, only a semi-infinite piezoelectric substrate has been considered [6], [7]. A review of different models has been presented by Szabo *et al.* [8].

In the case of a small piezoelectric coupling, the electric-field distribution is determined by considering the electric part of the problem only [9], [10]. In the present paper, we also consider the electric-field problem only. Our analysis has been inspired by Hartmann and Secrest [11]. These authors have presented a rather simple method to compute the electric field of an interdigital transducer in a two-media configuration. However, special measures have to be taken to avoid serious convergence problems. In the present paper, it is shown how to obtain optimum convergence. The latter is arrived at by minimization of the integrated square error made in the boundary conditions at the electroded surface. The number of layers is arbitrary. We assume that the principal axes of the permittivity tensor and the conductivity tensor coincide and that one of them is perpendicular to the interfaces of the layers, while the other is parallel to the fingers of the transducer. Further, the fingers are thought to be infinitely long (two-dimensional problem). A similar configuration has been investigated by Quak and Den Boon [12]. However, our present spectral iteration scheme is more flexible and leads to considerably smaller computation times. Finally, some numerical results for a realistic configuration [13] are presented to illustrate the power and versatility of the method and the pertinent computer program.

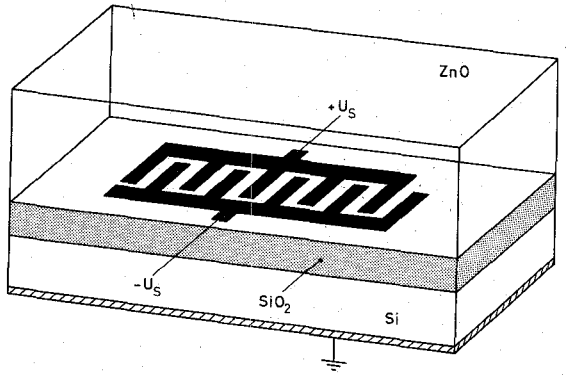

Fig. 1. A SAW device on a silicon substrate.

II. Description of the Configuration and the Electric-Field Problem

The general configuration to be investigated is shown in Fig. 2. A number of parallel electrodes with infinite electrical conductivity is situated in a plane interface of the multilayered structure. A Cartesian coordinate system (x, y, z) is introduced such that the electrodes are located in the plane $z = 0$ and parallel to the y-axis. The electroded part of the plane $z = 0$ is denoted as S, while the unelectroded part is denoted as S'. The part of S occupied by the pth electrode is called S_p and the part of S' adjoining the left edge of the pth electrode is called S_p'. The configuration consists of $M+1$ homogeneous layers at one side of the electroded plane and $N+1$ homogeneous layers at the other side. The interfaces between the layers are the planes $z = z_m$, $m = 1,2,\cdots, M$ for $z > 0$ and $z = z_n$, $n = 1,2,\cdots, N$ for $z < 0$.

The electric properties of a material can be characterized by its permittivity tensor ϵ and its conductivity tensor σ. We assume that in each layer the principal axis of ϵ and σ coincide with the axes of the Cartesian coordinate system. Then, in this system, both tensors are represented by the

Manuscript received February 28, 1984; revised August 7, 1984.
The authors are with the Department of Electrical Engineering, Delft University of Technology, 2600 GA Delft, The Netherlands.

0018-9480/85/0002-0121$01.00 ©1985 IEEE

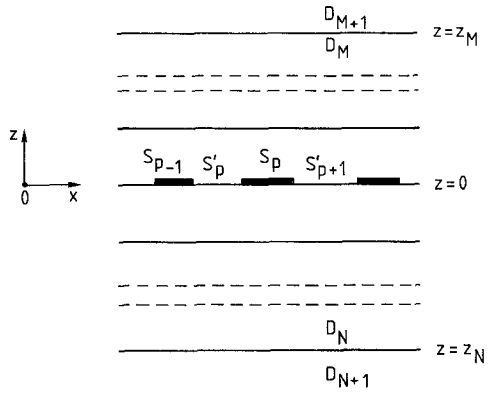

Fig. 2. The general configuration.

diagonal matrices

$$\epsilon = \begin{pmatrix} \epsilon_x & 0 & 0 \\ 0 & \epsilon_y & 0 \\ 0 & 0 & \epsilon_z \end{pmatrix} \qquad \sigma = \begin{pmatrix} \sigma_x & 0 & 0 \\ 0 & \sigma_y & 0 \\ 0 & 0 & \sigma_z \end{pmatrix}. \tag{1}$$

Sinusoidally time-varying voltages are applied to the electrodes and these generate a time-harmonic field. The complex time factor $\exp(j\omega t)$ is omitted in the formulas. In the range of frequencies we are interested in, we may neglect the influence of the magnetic field, so $\nabla \times \boldsymbol{E} = 0$, and hence the electric field can be written as

$$\boldsymbol{E} = -\nabla V \tag{2}$$

where V is the electric potential. From the (generalized) current density

$$\boldsymbol{J} = (\sigma + j\omega\epsilon)\cdot\boldsymbol{E} \tag{3}$$

and the equation of continuity

$$\nabla\cdot\boldsymbol{J} = 0 \tag{4}$$

together with (2), we obtain for each of the layers a partial differential equation to be satisfied by the electric potential

$$\nabla\cdot[(\sigma + j\omega\epsilon)\cdot\nabla V] = 0. \tag{5}$$

To determine V in each layer, we must further specify the boundary conditions at any interface. These conditions are as follows.

1) Across any interface, the electric potential V is continuous.
2) Across an unelectroded interface, the z-component J_z of the current density is continuous.
3) At the plane $z = 0$, the potential equals the prescribed constant value U_p at the pth electrode

$$V(x,0) = U_p, \qquad x \in S_p. \tag{6}$$

4) At the unelectroded part of $z = 0$, the jump in the z-component of the current density

$$[J_z(x)]_-^+ = \lim_{z\downarrow 0} J_z(x,z) - \lim_{z\uparrow 0} J_z(x,z) \tag{7}$$

is equal to zero

$$[J_z(x)]_-^+ = 0, \qquad x \in S'. \tag{8}$$

The electric current per unit length in the y-direction fed into the pth electrode follows from the surface integral of the z-component of the current density as

$$I_p = \int_{S_p} [J_z(x)]_-^+ \, dx. \tag{9}$$

The electrodes are fed in such a way that the net electric current in the configuration vanishes. Thus

$$\int_S [J_z(x)]_-^+ \, dx = 0. \tag{10}$$

As a consequence, the potential can be taken equal to zero as $|z| \to \infty$. In some applications, we are dealing with a perfectly conducting ground plane at $z = z_M$ and/or $z = z_N$. In the latter case, the potential at a ground-plane interface can also be taken equal to zero.

III. Spectral Representations

On account of the invariance of the configuration with respect to the y-coordinate, the electric-field problem is a two-dimensional one in x and z. We introduce the spatial Fourier transform of an arbitrary function $F(x,z)$ as

$$\tilde{F}(\alpha,z) = \int_{-\infty}^{\infty} F(x,z)\exp(-j\alpha x)\,dx, \qquad \alpha \in \mathbb{R} \tag{11}$$

while the original function $F(x,z)$ is found from the inverse transform as

$$F(x,z) = (2\pi)^{-1}\int_{-\infty}^{\infty} \tilde{F}(\alpha,z)\exp(j\alpha x)\,dx, \qquad x \in \mathbb{R}. \tag{12}$$

Similar Fourier transform pairs are defined for the potential $[V(x,z), \tilde{V}(\alpha,z)]$ and the current density $[\boldsymbol{J}(x,z), \tilde{\boldsymbol{J}}(\alpha,z)]$. With the aid of this Fourier transform, it is observed that (5) can be written as

$$-\kappa_x\alpha^2\tilde{V}(\alpha,z) + \kappa_z\partial_z^2\tilde{V}(\alpha,z) = 0 \tag{13}$$

where we have used $\partial_y = 0$. In (13), κ_x and κ_z are given by

$$\left.\begin{aligned} \kappa_{x,m} &= \epsilon_{x,m} + \sigma_{x,m}/j\omega \\ \kappa_{z,m} &= \epsilon_{z,m} + \sigma_{z,m}/j\omega \end{aligned}\right\} \text{ in } D_m \tag{14}$$

and

$$\left.\begin{aligned} \kappa_{x,n} &= \epsilon_{x,n} + \sigma_{x,n}/j\omega \\ \kappa_{z,n} &= \epsilon_{z,n} + \sigma_{z,n}/j\omega \end{aligned}\right\} \text{ in } D_n. \tag{15}$$

For the range of the subscripts we refer to Fig. 2.

It is now easily verified that the spectral solutions (in the α-domain) of (13) can be written in the matrix form

$$\begin{bmatrix} \tilde{V}(\alpha,z) \\ \tilde{J}_z(\alpha,z) \end{bmatrix} = [\mathrm{T}_m(\alpha, z-z')]\begin{bmatrix} \tilde{V}(\alpha,z') \\ \tilde{J}_z(\alpha,z') \end{bmatrix} \text{ in } D_m \quad (m = 1,2,\cdots,M) \tag{16}$$

where the transfer matrix is given by

$$[\mathrm{T}_m(\alpha,z)] = \begin{bmatrix} \cosh(\gamma_m z) & -Y_m^{-1}\sinh(\gamma_m z) \\ -Y_m\sinh(\gamma_m z) & \cosh(\gamma_m z) \end{bmatrix} \tag{17}$$

in which

$$\gamma_m(\alpha) = |\alpha|(\kappa_{x,m}/\kappa_{z,m})^{1/2} \qquad (m=1,2,\cdots,M+1) \quad (18)$$

$$Y_m(\alpha) = j\omega|\alpha|(\kappa_{x,m}\kappa_{z,m})^{1/2} \qquad (m=1,2,\cdots,M+1) \quad (19)$$

the square roots being defined as $\mathrm{Re}(\cdots)^{1/2} \geqslant 0$. Similar relations in D_n are arrived at if, in (16)–(19), m is replaced by n and M is replaced by N.

The boundary conditions at the unelectroded interfaces are simply the relations

$$\lim_{z \uparrow z_m} \begin{bmatrix} \tilde{V}(\alpha, z) \\ \tilde{J}_z(a, z) \end{bmatrix} = \lim_{z \downarrow z_m} \begin{bmatrix} \tilde{V}(\alpha, z) \\ \tilde{J}_z(a, z) \end{bmatrix} \qquad (m=1,2,\cdots,M) \quad (20)$$

$$\lim_{z \downarrow z_n} \begin{bmatrix} \tilde{V}(\alpha, z) \\ \tilde{J}_z(a, z) \end{bmatrix} = \lim_{z \uparrow z_n} \begin{bmatrix} \tilde{V}(\alpha, z) \\ \tilde{J}_z(a, z) \end{bmatrix} \qquad (n=1,2,\cdots,N). \quad (21)$$

In the semi-infinite domain D_{M+1}, we have solutions of (13) of the type $\exp(-\gamma_{M+1}z)$; hence, at the interface $z = z_M$, we have the relation

$$\tilde{J}_z(\alpha, z_M) = Y_{M+1}\tilde{V}(\alpha, z_M). \quad (22a)$$

If the plane $z = z_M$ is grounded, then, simply

$$\tilde{V}(\alpha, z_M) = 0. \quad (22b)$$

In the semi-infinite domain D_{N+1}, we have solutions of (13) of the type $\exp(\gamma_{N+1}z)$; hence, at the interface $z = z_N$, we have the relation

$$\tilde{J}_z(\alpha, z_N) = -Y_{N+1}\tilde{V}(\alpha, z_N). \quad (23a)$$

If the plane $z = z_N$ is grounded, then, simply

$$\tilde{V}(\alpha, z_N) = 0. \quad (23b)$$

Now, using the transfer-matrix formulation of (17) and (20), the spectral representation of the potential $\tilde{V}(\alpha,0^+) = \lim_{z \downarrow 0}\tilde{V}(\alpha, z)$ and the current density $\tilde{J}_z(\alpha,0^+) = \lim_{z \downarrow 0} \tilde{J}_z(\alpha, z)$ can be expressed in the pertaining values at $z = z_M$ as

$$\begin{bmatrix} \tilde{V}(\alpha,0^+) \\ \tilde{J}_z(\alpha,0^+) \end{bmatrix} = [T_{1\to M}] \begin{bmatrix} \tilde{V}(\alpha, z_M) \\ \tilde{J}_z(\alpha, z_M) \end{bmatrix} \quad (24)$$

where the elements of the transfer matrix $[T_{1\to M}]$ follow from

$$\begin{bmatrix} T_{1\to M}^{(1,1)} & T_{1\to M}^{(1,2)} \\ T_{1\to M}^{(2,1)} & T_{1\to M}^{(2,2)} \end{bmatrix} = \prod_{m=1}^{M} [T_m(\alpha, z_{m-1} - z_m)]. \quad (25)$$

Similarly, the spectral representation of the potential $\tilde{V}(\alpha,0^-) = \lim_{z \uparrow 0}\tilde{V}(\alpha, z)$ and the current density $\tilde{J}_z(\alpha,0^-) = \lim_{z \uparrow 0}\tilde{J}_z(\alpha, z)$ can be expressed in the pertaining values at $z = z_N$ as

$$\begin{bmatrix} \tilde{V}(\alpha,0^-) \\ \tilde{J}_z(\alpha,0^-) \end{bmatrix} = [T_{1\to N}] \begin{bmatrix} \tilde{V}(\alpha, z_N) \\ \tilde{J}_z(\alpha, z_N) \end{bmatrix} \quad (26)$$

where

$$\begin{bmatrix} T_{1\to N}^{(1,1)} & T_{1\to N}^{(1,2)} \\ T_{1\to N}^{(2,1)} & T_{1\to N}^{(2,2)} \end{bmatrix} = \prod_{n=1}^{N} [T_n(\alpha, z_{n-1} - z_n)]. \quad (27)$$

Combining (22) and (24), we arrive at

$$\tilde{J}_z(\alpha,0^+) = Y^+(\alpha)\tilde{V}(\alpha,0^+) \quad (28)$$

where

$$Y^+(\alpha) = \frac{T_{1\to M}^{(2,1)} + Y_{M+1}T_{1\to M}^{(2,2)}}{T_{1\to M}^{(1,1)} + Y_{M+1}T_{1\to M}^{(1,2)}} \quad (29a)$$

or, if the plane $z = z_M$ is grounded

$$Y^+(\alpha) = T_{1\to M}^{(2,2)} / T_{1\to M}^{(1,2)}. \quad (29b)$$

It is noted that, in case we are dealing with only a semi-infinite medium present for $z > 0$, we have $Y^+(\alpha) = Y_m(\alpha)$, where $m = 1$. Similarly, the combination of (23) and (26) leads to

$$\tilde{J}_z(\alpha,0^-) = -Y^-(\alpha)\,\tilde{V}(\alpha,0^-) \quad (30)$$

where

$$Y^-(\alpha) = -\frac{T_{1\to N}^{(2,1)} - Y_{N+1}T_{1\to N}^{(2,2)}}{T_{1\to N}^{(1,1)} - Y_{N+1}T_{1\to N}^{(1,2)}} \quad (30a)$$

or, if the plane $z = z_N$ is grounded

$$Y^-(\alpha) = T_{1\to N}^{(2,2)} / T_{1\to N}^{(1,2)}. \quad (30b)$$

It is noted that, in case we are dealing with only a semi-infinite media present for $z < 0$, we have $Y^-(\alpha) = Y_n(\alpha)$, where $n = 1$.

Finally, the spectral relation between the potential $\tilde{V}(\alpha,0) = \tilde{V}(\alpha,0^+) = \tilde{V}(\alpha,0^-)$ and the jump in the z-component of the current density $[\tilde{J}_z(\alpha)]_-^+ = \tilde{J}_z(\alpha,0^+) - \tilde{J}_z(\alpha,0^-)$ is obtained by combining (28) and (30). We arrive at

$$[\tilde{J}_z(\alpha)]_-^+ = Y(\alpha)\tilde{V}(\alpha,0) \quad (31)$$

with

$$Y(\alpha) = Y^+(\alpha) + Y^-(\alpha). \quad (32)$$

The only conditions yet to be fullfilled are (6)–(10). Thus, the electric-field problem as described in Section II has been reduced to a dual boundary value problem for the potential in $z = 0$ and the jump in the z-component of the current density in $z = 0$, where (31) is an interconnecting relation between these quantities. Once this one-dimensional problem for $z = 0$ has been solved, the potential can be determined in whole space $\mathbb{R}^2$. The latter directly follows from (28) and (30) and the transfer-matrix technique of (16)–(21). Finally, the electric field is obtained from (2).

IV. Iterative Minimization of the Integrated Square Error

This section outlines the iterative method used to find a solution to the problem described by the spectral relation of (31) and the dual boundary value problem of (6) and (8). Further, (10) should be satisfied as well.

A. Initial Estimate

The method starts with an initial estimate for which the current density satisfies all conditions. A simple choice is

the constant value

$$V^{(0)}(x,0) = \int_S U_p\,dx' \Big/ \int_S dx', \qquad x \in \mathbb{R} \tag{33}$$

being the integrated average value over all electrodes. The related jump in the current density $[J_z(x)]_-^+$ is identical equal to zero and satisfies (8) and (10) trivially.

B. Iterative Procedure

In order to fulfill (6), we have an iterative procedure where the nth estimate of the potential $V^{(n)}(x,0)$ is generated from the former step of the iteration as

$$V^{(n)}(x,0) = V^{(n-1)}(x,0) + \eta^{(n)} v^{(n)}(x), \qquad x \in \mathbb{R} \tag{34}$$

where $\eta^{(n)}$ is a complex variational parameter and $v^{(n)}(x)$ is a suitably chosen variational potential. The current density $[J_z(x)]_-^+$ related to this variational potential $v^{(n)}(x)$ through (31) should satisfy (8) and (10). Notice that the current density related to $V^{(n)}$ then satisfies (8) and (10). The actual construction of $v^{(n)}(x)$ will be discussed in Section V. The deviation of the estimated potential $V^{(n)}(x)$ from the required value U_p at the pth electrode is denoted by $F^{(n)}(x)$ as

$$F^{(n)}(x) = U_p - V^{(n)}(x,0), \qquad x \in S_p \tag{35}$$

while the integrated square error $ERR^{(n)}$ after n steps is given by

$$ERR^{(n)} = \int_S \left| F^{(n)}(x) \right|^2 dx. \tag{36}$$

The expression for $ERR^{(n)}$ can now be written as

$$ERR^{(n)} = ERR^{(n-1)} - 2\,\mathrm{Re}\left[\eta^{(n)*} A^{(n)}\right] + \left|\eta^{(n)}\right|^2 B^{(n)} \tag{37}$$

in which

$$A^{(n)} = \int_S v^{(n)*}(x) F^{(n-1)}(x)\,dx \tag{38}$$

and

$$B^{(n)} = \int_S \left| v^{(n)}(x) \right|^2 dx. \tag{39}$$

The right-hand side of (37) has, as a function of $\eta^{(n)}$, a minimum at

$$\eta^{(n)} = A^{(n)} / B^{(n)}. \tag{40}$$

Taking $\eta^{(n)}$ to be this value in (37), we obtain

$$ERR^{(n)} = ERR^{(n-1)} - \left|A^{(n)}\right|^2 / B^{(n)} \tag{41}$$

from which it follows that, if $A^{(n)} \neq 0$, $ERR^{(n)} < ERR^{(n-1)}$. In this way, a possible divergence of the iteration scheme has been excluded.

A necessary but not sufficient condition that $ERR^{(n)} = 0$ for some n is

$$\int_S F^{(n)}(x)\,dx = 0. \tag{42}$$

For $n = 0$, our choice of the initial estimate of (33) satisfies this condition already. Therefore, we employ

$$\int_S v^{(n)}(x)\,dx = 0 \tag{43}$$

as an extra condition for the selection of the variational potential (cf., Section V).

C. Second Minimization Step

In order to decrease the right-hand side of (37) still further by manipulating the variational potential $v^{(n)}$, we substitute (40) in (34) and use the expressions for $A^{(n)}$ and $B^{(n)}$. Then, it follows that

$$\int_S v^{(q)*}(x) F^{(q)}(x)\,dx = 0, \qquad q = 1,2,\cdots,n. \tag{44}$$

With this orthogonality relation, we are now able to minimize $B^{(n)}$, while keeping $A^{(n)}$ unchanged if, in the right-hand side of (39), the function $v^{(n)}(x)$ is replaced by $v^{(n)}(x) - \zeta^{(n)} v^{(n-1)}(x)$, where $\zeta^{(n)}$ is a second variational parameter. If this replacement is carried out in (39), a new value $\bar{B}^{(n)}$ of $B^{(n)}$ is constructed, that follows as

$$\bar{B}^{(n)} = B^{(n)} - 2\,\mathrm{Re}\left[\zeta^{(n)*} C^{(n)}\right] + \left|\zeta^{(n)}\right|^2 B^{(n-1)} \tag{45}$$

where

$$C^{(n)} = \int_S v^{(n-1)*}(x) v^{(n)}(x)\,dx. \tag{46}$$

The right-hand side of (45) has as a function of $\zeta^{(n)}$ a minimum at

$$\zeta^{(n)} = C^{(n)} / B^{(n-1)}. \tag{47}$$

Taking, in (45), $\zeta^{(n)}$ to be this value, we arrive at

$$\bar{B}^{(n)} = B^{(n)} - \left|C^{(n)}\right|^2 / B^{(n-1)}. \tag{48}$$

First of all, this shows that $\bar{B}^{(n)} < B^{(n)}$, if $C^{(n)} \neq 0$. Further, it follows by substituting (47) in

$$\bar{v}^{(n)}(x) = v^{(n)}(x) - \zeta^{(n)} v^{(n-1)}(x), \qquad x \in \mathbb{R} \tag{49}$$

that

$$\int_S v^{(n-1)*}(x) \bar{v}^{(n)}(x)\,dx = 0. \tag{50}$$

If the original function $v^{(n)}(x)$ was already such that the right-hand side of (46) vanished, then no improvement will be attained in this second minimization step. Note that this is consistent with (50). Hence, the second minimization step automatically stops after being carried out once. In the next section, we shall discuss a procedure that leads, in each iteration, to the generation of a particular value of $v^{(n)}(x)$. Once $\zeta^{(n)}$ has been determined, $v^{(n)}(x)$ can be replaced by $\bar{v}^{(n)}(x)$ of (49). Note that the second minimization step can only be carried out from $n = 2$ onward, since $v^{(0)}$ is not defined. The complete iteration scheme is shown in Table I.

V. Generation of the Variational Potentials

This section presents the technique to construct the variational potential $v^{(n)}(x)$ such that in the α-domain we

TABLE I
THE ITERATION SCHEME

$$V^{(0)}(x,0) = \int_S U_p\,dx' \,/\, \int_S dx'$$

$n=0$

$$F^{(0)}(x) = U_p - V^{(0)}(x,0)$$

$$ERR^{(0)} = \int_S |F^{(0)}(x)|^2\,dx$$

$n=n+1$

determination of $v^{(n)}(x)$ (Section V)

$$A^{(n)} = \int_S v^{(n)*}(x)\,F^{(n-1)}(x)\,dx$$

$$B^{(n)} = \int_S |v^{(n)}(x)|^2\,dx$$

if $n>1$

$$C^{(n)} = \int_S v^{(n-1)*}(x)\,v^{(n)}(x)\,dx$$

$$\zeta^{(n)} = C^{(n)} \,/\, B^{(n-1)}$$

$$B^{(n)} := B^{(n)} - \zeta^{(n)}\,C^{(n)*}$$

$$v^{(n)}(x) := v^{(n)}(x) - \zeta^{(n)}\,v^{(n-1)}(x)$$

$$\eta^{(n)} = A^{(n)} \,/\, B^{(n)}$$

$$V^{(n)}(x,0) = V^{(n-1)}(x,0) + \eta^{(n)}\,v^{(n)}(x)$$

$$F^{(n)}(x) = U_p - V^{(n)}(x,0)$$

$$ERR^{(n)} = \int_S |F^{(n)}(x)|^2\,dx$$

have a spectral relation equivalent to (31) as

$$\tilde{j}_z^{(n)}(\alpha) = Y(\alpha)\,\tilde{v}^{(n)}(\alpha) \tag{51}$$

where, in the x-domain

$$j_z^{(n)}(x) = 0, \qquad x \in S' \tag{52}$$

$$\int_S j_z^{(n)}(x)\,dx = 0 \tag{53}$$

$$\int_S v^{(n)}(x)\,dx = 0. \tag{54}$$

A suitable choice of $v^{(n)}$ would be

$$v^{(n)}(x) = \begin{cases} F^{(n-1)}(x), & x \in S \\ 0, & x \in S' \end{cases}. \tag{55}$$

Clearly, the choice of $v^{(n)}(x)$ at S provides an error $ERR^{(n)} = 0$, but (51)–(54) have not necessarily been met. Table II shows how a variational potential with an associated $j_z^{(n)}$ satisfying all requirements can be generated by using the value $v^{(n)}$ of (55) as a starting point. In step (a) of Table II, the current-density jump that is related to the potential of (55) is determined. Subsequently, in step (b),

TABLE II
GENERATION OF $v^{(n)}(x)$, $x \in \mathbb{R}$

	x-domain ($x \in \mathbb{R}$)		α-domain ($\alpha \in \mathbb{R}$)
(a)	$F^{(n-1)}(x)$, $x \in S$; 0, $x \in S'$	$\Longrightarrow$	$\tilde{F}_S(\alpha)$
	$j_z^{(n)}(x)$	$\Longleftarrow$	$\tilde{j}_z^{(n)}(\alpha) = Y(\alpha)\,\tilde{F}_S(\alpha)$
(b)	$j_z^{(n)}(x) := 0$, $x \in S'$; $j_z^{(n)}(x) - \dfrac{\int_S j_z^{(n)}(x')\,dx'}{\int_S dx'}$, $x \in S$		
(c)	$j_z^{(n)}(x)$	$\Longrightarrow$	$\tilde{j}_z^{(n)}(\alpha)$
	$v^{(n)}(x)$	$\Longleftarrow$	$\tilde{v}^{(n)}(\alpha) = \tilde{j}_z^{(n)}(\alpha)/Y(\alpha)$, $\alpha \in \mathbb{R}\setminus\{0\}$; 0, $\alpha=0$
(d)	$v^{(n)}(x) := v^{(n)}(x) - \dfrac{\int_S v^{(n)}(x')\,dx'}{\int_S dx'}$		

the current-density jump is forced to satisfy (52) and (53) by simply setting the value of this function at the unelectroded part S' as well as the average value at the electroded part S at zero. In step (c), the potential results such that the average value of this potential over $\mathbb{R}$ is zero. In the last step (d), $v^{(n)}$ is constructed such that this function satisfies (54). Note that this last modification of $v^{(n)}$ does not modify the related $j_z^{(n)}$. In the spectral relation of (51), only $\tilde{v}^{(n)}(0)$ would change; however, this has no influence upon $\tilde{j}_z^{(n)}(0)$, since we know that $Y(0) = 0$.

VI. COMPUTATIONAL ASPECTS AND NUMERICAL RESULTS

In our computational approach, we represent all spatial functions occurring in the iteration scheme as functions of certain discrete values of x, while in the Fourier domain, all spectral functions are represented as functions of certain discrete values of α. The Fourier transform and the inverse Fourier transform in discrete form between the spatial and the spectral functions are performed by the very efficient fast Fourier transform (FFT) technique [14]. In order to implement the FFT technique, we have to recognize that, in fact, the FFT can only be applied to periodic functions. This implies that only the electric-field problem of an infinite periodic interdigital transducer can be solved. It is obvious that a finite interdigital transducer having a large number of periodically located electrodes is very similar to an infinite periodic one. If this assumption is not valid, then the interdigital transducer can be simulated as an infinite periodic one of which the period

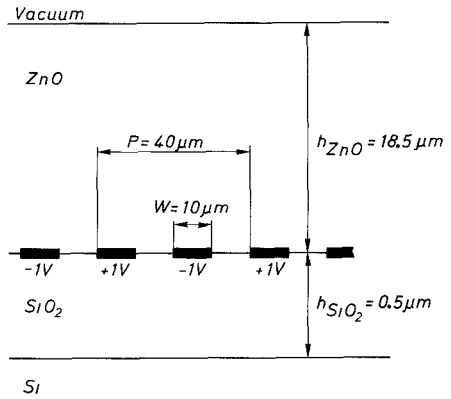

Fig. 3. An interdigital metal pattern in a vacuum ZnO–SiO_2–Si configuration.

TABLE III
THE VALUES OF THE RELATIVE PERMITTIVITIES ($\epsilon_r = \epsilon/\epsilon_0$; $\epsilon_0 = 8.854\ 10^{-12}$ F/m) AND CONDUCTIVITIES OF THE MEDIA OF THE CONFIGURATION OF FIG. 3

medium	$\epsilon_{x,r}$	$\epsilon_{z,r}$	σ_x in S/m	σ_z in S/m
Vacuum	1	1	0	0
ZnO	8.32	8.83	0	0
SiO_2	3.78	3.78	0	0
Si	11.7	11.7	1.0	1.0

TABLE IV
THE ROOT-MEAN-SQUARE ERROR AS A FUNCTION OF THE NUMBER OF ITERATIONS

Iteration step	The root mean square error $\omega = 10^6$	$\omega = 10^{10}$
1	13 %	12 %
2	0.074 %	0.15 %
3	0.021 %	0.10 %
4	0.0017 %	0.01 %
5	0.0004 %	0.005 %

consists of the interdigital transducer involved supplemented with a large unelectroded surface. In this way, the mutual influence of two adjacent periods is reduced. Further in our computational approach, all integrations over S in the iteration scheme are replaced by a simple numerical summation (trapezoidal integration rule).

In order to demonstrate the performance of the presented method, we apply it to a specific configuration (Fig. 3). It consists of an infinite periodic interdigital metal pattern in a vacuum ZnO–SiO_2–Si structure. The polarities of the fingers are alternately +1 V and −1 V. All electroded domains ($=W$) and all unelectroded domains are equally sized. The period ($=P$) of the interdigital transducer, being the distance between the left edges of two adjacent positive electrodes, is taken 40 μm. Table III lists the relative permittivities and the conductivities of the media of the configuration in Fig. 3. In Table IV, we present the values of the root-mean-square error $[ERR^{(n)}/\int_S dx]^{1/2}$ as a function of the number of iterations. The remarkable convergence of the present iterative method has to be noted.

In Fig. 4, we present the numerical results for the spatial distribution of the potential and the surface charge $\rho_s = (j\omega)^{-1}[J_z(x)]_-^+$ at the electroded plane of the configuration of Fig. 3. The frequencies of operation are taken to be $\omega = 10^6$ rad/s (curve a) and $\omega = 10^{10}$ rad/s (curves b and c). The surface charge in the low-frequency situation is larger than in the high-frequency one. Furthermore, the surface charge as well as the potential at the electroded plane are approximately real in the low-frequency case, and become complex when the frequency is increased. The isopotential plots of Fig. 5 also visualize the difference between the high- and the low-frequency behavior. For $\omega = 10^6$ rad/s, it is observed that the isopotential lines do not penetrate into the silicon bulk. Replacing the silicon medium by a highly conductive plate, we have observed no difference in the isopotential plots of the two configurations for this low-frequency region. For $\omega = 10^{10}$ rad/s, the isopotential lines penetrate into the silicon. The discontinuities in the curves at the interfaces are due to continuity constraints of the potential and the normal component of the current density. In Fig. 6, the frequency behavior of the

The configuration of Fig. 3 has a discretization of 256 points within the period P.

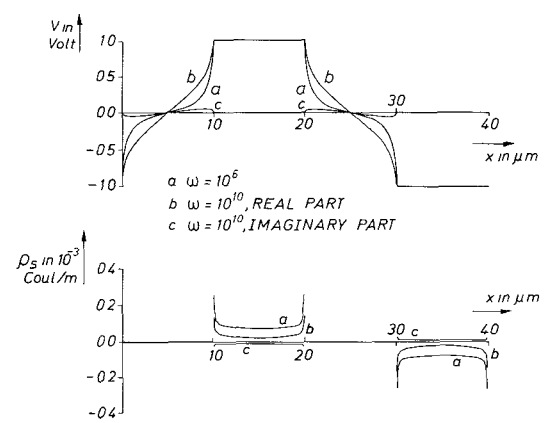

Fig. 4. The spatial distribution of the potential and surface charge at the electroded plane of the configuration of Fig. 3.

configuration is further visualized by the capacitance and the conductance of a finger pair as a function of the frequency. It is observed that the conductance G (= the quotient of the real part of the current through one electrode and the pertaining potential difference of the finger pair) is practically zero for low frequencies, while the capacitance C (= the quotient of the real part of the surface charge at one electrode and the pertaining potential difference of the finger pair) has a constant value. At high

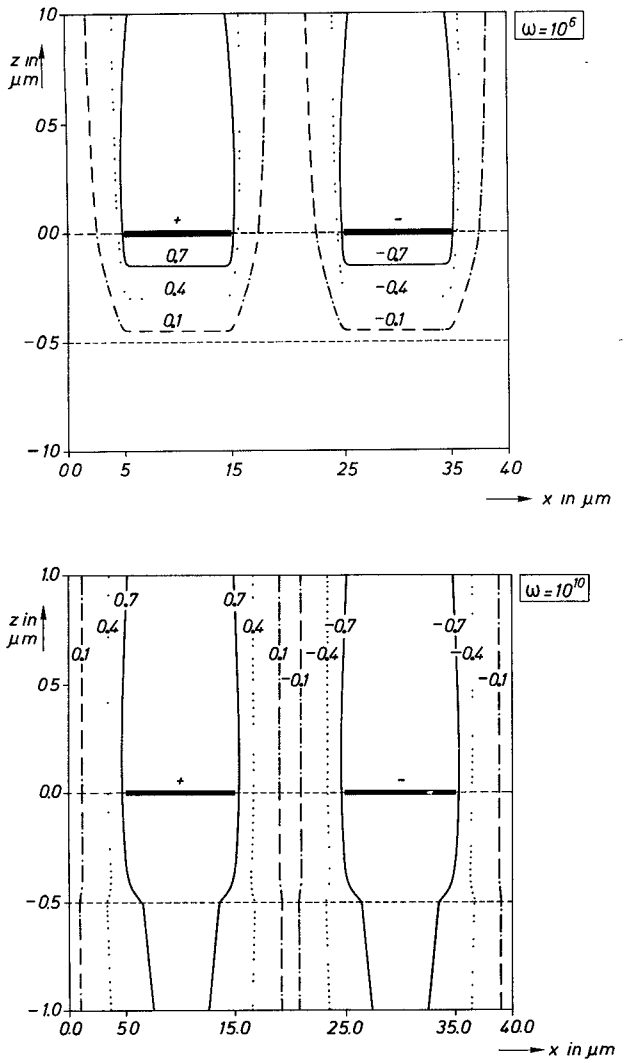

Fig. 5. The potential distribution in the configuration of Fig. 3 for $\omega = 10^6$ and $\omega = 10^{10}$.

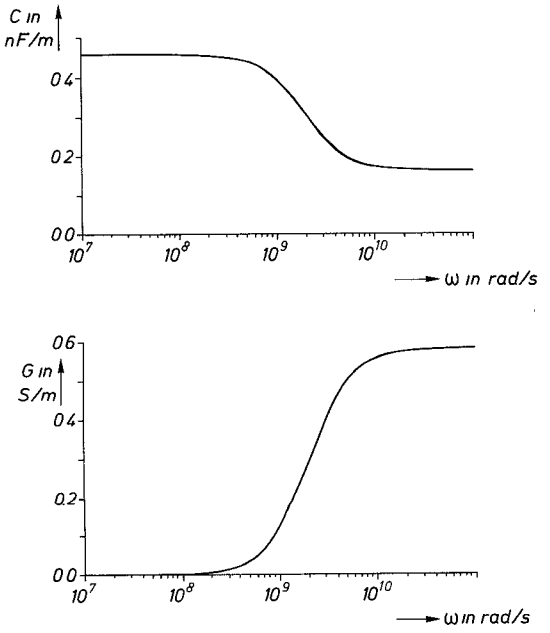

Fig. 6. The capacitance and conductance of a finger pair as function of the frequency.

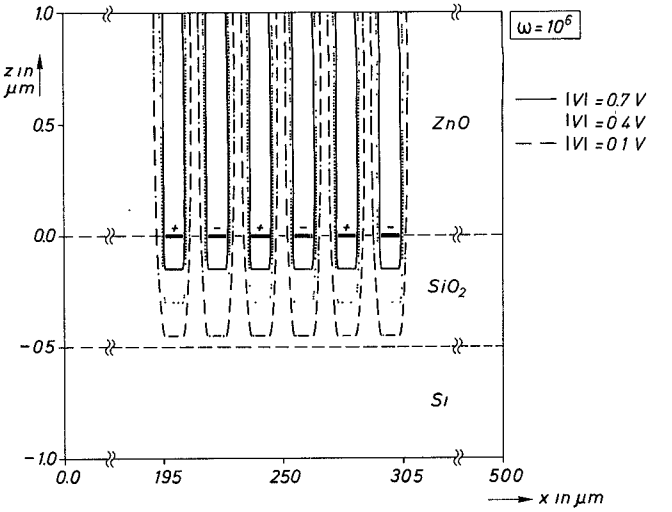

Fig. 7. The potential distribution in the configuration of Fig. 3, while the metal pattern consists of six electrodes only ($\omega = 10^6$).

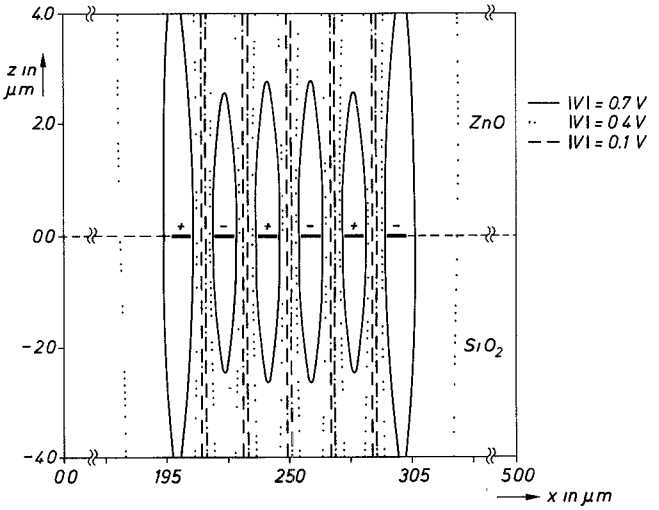

Fig. 8. The potential distribution in the configuration of Fig. 3, while the thickness of the SiO_2 layer is infinite ($h_{SiO_2} \to \infty$) and the metal pattern consists of six electrodes only.

frequencies, the capacitance has a smaller constant value, and the conductance is not negligible anymore. In Fig. 7, we present the isopotential lines of a finite interdigital metal pattern of six electrodes in the vacuum ZnO–SiO_2–Si structure of Fig. 3. To simulate the infinite domain in which the six electrodes have been situated, we take a period (in the FFT calculations) of fifty times the width of one electrode. Fig. 7 demonstrates that the influence of end effects in this configuration are negligible. In Fig. 8, we show an isopotential plot for the metal pattern of six electrodes in the configuration of Fig. 3, while the thickness of the SiO_2 layer is thought to be infinite ($h_{SiO_2} \to \infty$). Here, the end effects play a dominant role. Obviously, the conductivity of the silicon substrate in Fig. 7 has reduced the influence of end effects.

In order to discuss the influence of the discretization upon our numerical results, we therefore compare our numerical results to known analytical ones in a simple

TABLE V
THE RELATIVE ERROR AND THE COMPUTATION TIME (ON AN AMDAHL V/7-B COMPUTER) RESULTING FROM THE COMPUTATION OF THE CAPACITANCE OF A PERIODIC INTERDIGITAL TRANSDUCER IN VACUUM

Number of points	Relative error	Computation time
32	3 %	< 1 s
64	1.6 %	< 1 s
128	0.7 %	1 s
256	0.3 %	1 s
512	0.1 %	4 s
1024	0.02 %	7 s

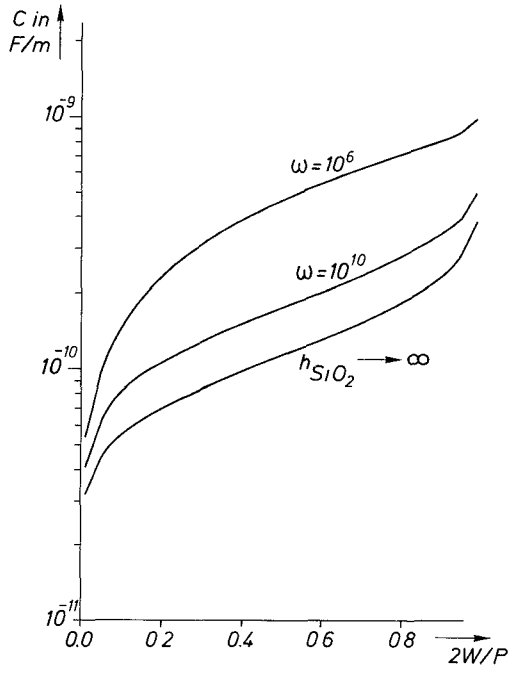

Fig. 9. The capacitance of a finger pair in the configuration of Fig. 3 as a function of the electrode width (W), while the period P is constant.

configuration of an infinite periodic metal pattern in vacuum. The capacitance is then given by [9]

$$C = 2\epsilon_0 K(k)/K\left((1-k^2)^{1/2}\right) \tag{56}$$

where K is the complete elliptic integral of the first kind [15], and $k = \cos(1/2\pi(1-2W/P))$. Table V presents the relative error as a function of the number N of discretization points within a period P, where the summed square error of the discretized iteration scheme is negligible.

Finally, the capacitance pertaining to the configuration of Fig. 3 as a function of W is presented in Fig. 9. Additionally, we also present the capacitance if the thickness of the SiO_2 layer is thought to be infinite.

VII. CONCLUSIONS

We have presented a computational method to investigate the behavior of a SAW transducer. The method is based upon a fast convergent iterative scheme. The minimization of the error made in the satisfaction of the boundary condition at the electrodes has guaranteed the convergence of the scheme. Using the FFT technique, the numerical computations are straightforward. At this moment, we are now able to compute the electric field of any realistic finger structure in any realistic layered environment.

We have further shown that the influence of the layers is necessary to take into account. A conducting layer can influence the mutual coupling of the transducer fingers dramatically.

REFERENCES

[1] R. N. Thurston, "Wave propagation in fluids and normal solids," in *Physical Acoustics*, part IA, W. P. Mason, Ed. New York: Academic Press, 1964, ch. 1, pp. 1–110.
[2] D. A. Berlincourt, D. R. Curran, and H. Jaffe, "Piezoelectric and piezomagnetic materials and their function in transducers," in *Physical Acoustics*, part IA, W. P. Mason, Ed. New York: Academic Press, 1964, ch. 3, pp. 169–270.
[3] W. R. Smith *et al.*, "Analysis of interdigital surface wave transducers by use of an equivalent circuit model," *IEEE Trans. Microwave Theory Tech.*, vol. MTT-17, pp. 856–864, Nov. 1969.
[4] W. R. Smith and W. F. Pedler, "Fundamental- and harmonic-frequency circuit-model analysis of interdigital transducers with arbitrary metallization ratios and polarity sequences," *IEEE Trans. Microwave Theory Tech.*, vol. MTT-23, pp. 853–864, Nov. 1975.
[5] B. A. Auld and G. S. Kino, "Normal mode theory for acoustic waves and its application to the interdigital transducer," *IEEE Trans. Electron Devices*, vol. ED-18, pp. 898–908, Oct. 1971.
[6] A. K. Ganguly and M. O. Vassell, "Frequency response of acoustic surface wave filters. Part I," *J. Appl. Phys.*, vol. 44, pp. 1072–1085, Mar. 1973.
[7] R. F. Milson, N. H. C. Reilly, and M. Redwood, "Analysis of generation and detection of surface and bulk acoustic waves by interdigital transducers," *IEEE Trans. Sonics Ultrason.*, vol. SU-24, pp. 147–166, May 1977.
[8] T. L. Szabo, K. R. Laker, and E. Cohen, "Interdigital transducer models: Their impact on filter synthesis," *IEEE Trans. Sonics Ultrason.*, vol. SU-26, pp. 321–333, Sept. 1979.
[9] H. Engan, "Excitation of elastic surface waves by spatial harmonics of interdigital transducers," *IEEE Trans. Electron Devices*, vol. ED-16, pp. 1041–1017, Dec. 1969.
[10] G. W. Farnell, I. A. Cermak, P. Silvester, and S. K. Wong, "Capacitance and field distributions for interdigital surface-wave transducers," *IEEE Trans. Sonics Ultrason.*, vol. SU-17, pp. 188–195, July 1970.
[11] C. S. Hartmann and B. C. Secrest, "End effects in interdigital surface wave transducers," in *1972 Ultrasonics Symp. Proc.*, IEEE Cat. no. 72-CHD-8SU, 1972, pp. 413–416.
[12] D. Quak and G. den Boon, "Electric input admittance of an interdigital transducer in a layered, anisotropic, semiconducting structure," *IEEE Trans. Sonics Ultrason.*, vol. SU-25, pp. 44–50, Jan. 1978.
[13] W. J. Ghijsen and A. Venema, "Optimal transducer design for the generation of SAW in silicon substrates," *Sensors and Actuators*, vol. 3, pp. 51–62, 1982/1983.
[14] E. O. Brigham, *The Fast Fourier Transform*. Englewood Cliffs, NJ: Prentice-Hall, 1974, pp. 1–252.
[15] M. Abramowitz and I. A. Stegun, *Handbook of Mathematical Functions*. Washington DC: National Bureau of Standards, 1964, ch. 17, pp. 587–626.

Peter M. van den Berg was born in Rotterdam, The Netherlands, on November 11, 1943. He received a degree in electrical engineering from the Polytechnic School of Rotterdam in 1964. He received the B.Sc. and M.Sc. degrees in electrical engineering from The Delft University of Technology, The Netherlands, in 1966 and 1968, respectively, and the Ph.D. degree in technical sciences from The Delft University of Technology, in 1971.

From 1967 to 1968, he was employed as a Research Engineer by the Dutch Patent Office. From 1968 until the present, he has been a member of the Scientific Staff of the Electromagnetic Research Group of The Delft University of Technology. During these years, he carried out research and taught classes in the area of wave propagation and scattering problems. During the academic year 1973–1974, he was a Visiting Lecturer in the Department of Mathematics, University of Dundee, Scotland. During a three-month's period of 1980–1981, he was a Visiting Scientist at the Institute of Theoretical Physics, Goteborg, Sweden. He was appointed Professor at The Delft University of Technology in 1981.

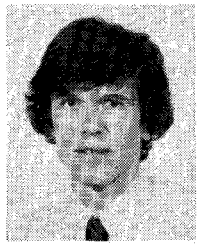

Walter J. Ghijsen was born in Geldrop, The Netherlands, on June 24, 1958. He received the M.Sc. degree in electrical engineering in 1983 from The Delft University of Technology, Delft, The Netherlands. He is currently working towards his Ph.D. degree in technical sciences at The Delft University of Technology.

✤

Adrian Venema (M'82) was born in Cimahi, Indonesia, in 1932. He received the B.Sc. electrical engineering degree in 1954 from the Polytechnic School in Leeuwarden. He received the M.Sc. and Ph.D. degrees in electrical engineering from The Delft University of Technology in 1968 and 1980, respectively.

He is a senior staff member of the Electronic Instrumentation Laboratory of the Electrical Engineering Department. He is currently responsible for research in SAW devices in silicon.

Computer Calculation of Large-Signal GaAs FET Amplifier Characteristics

ANDRZEJ MATERKA AND TOMASZ KACPRZAK

Abstract—**A simple and efficient method of GaAs FET amplifier analysis is presented. The FET is represented by its circuit-type nonlinear dynamic model taking into account the device's main nonlinear effects including gate–drain voltage breakdown. An identification procedure for extraction of the model parameters is described in detail and examples are given. The calculation of the amplifier response to a single-input harmonic signal is performed using the piecewise harmonic balance technique. As this technique is rather time-consuming in its original form, the optimization routine used to solve the network equations was replaced by the Newton–Raphson algorithm. Characteristics calculated with the use of the proposed method are compared with experimental data taken for a microwave amplifier using a 2SK273 GaAs FET unit. Good agreement at 9.5 GHz over wide ranges of bias voltage and input power levels are observed.**

I. Introduction

THE GaAs FET is receiving continuously growing attention from circuit designers both in low-noise and high-power applications. Particularly, the power FET is an attractive device for use in microwave amplifiers and oscillators with its efficiency and power performance comparable or even superior to the other commercial solid-state or TWT sources. On the other hand, the power FET has received much less attention from researchers than its low-noise counterpart and, still, there is a need for data on device RF characterization at large-signal drive levels.

Manuscript received November 10, 1983; revised September 17, 1984.

The authors are with the Technical University of Łódź, Institute of Electronics, Gdanska Street 176, 90-924 Łódź, Poland.

Some efforts have been made to simulate the large-signal GaAs MESFET performance based on the numerical solution of the two-dimensional nonlinear differential equations describing the electron transport in the channel. The numerical results [1] are very helpful to understand device operation, but long computational time makes this approach impractical in circuit analysis and design programs. Recently, Madjar and Rosenbaum [2], [3] and Shur and Eastman [4] developed approximate analytical theories to model the active region under the gate of the microwave GaAs FET. Although one of these theories has been applied to the analysis of a practical microwave FET oscillator [3], both of them are of limited use in circuit design practice because they utilize the FET physical parameters which are scarcely available to the circuit designers. Willing, Rauscher, and de Santis [5] characterized an actual device with a quasi-static approach by measuring small-signal scattering parameters at a number of operating points to formulate an equivalent circuit, some of whose elements are bias-dependent. They use polynomial forms to approximate these dependences and a time-domain analysis program to calculate the large-signal device characteristics. The results obtained compare favorably with the experimentally determined characteristics, but the complexity of the equivalent circuit makes the identification technique of the model parameters rather laborious. Later, Rauscher [6]

0018-9480/85/0002-0129$01.00 ©1985 IEEE